Applied and Computational Mathematics
2026; 15(1): 1-12
http://www.sciencepublishinggroup.com/j/acm
doi: 10.11648/j.acm.20261501.11

Study of Coupled Water-Sediment Energy Dynamics in Dam-Driven Closed-Conduit Flows

Doglas Ambani Onchere*, Mathew Ngugi Kinyanjui, Phineas Roy Kiogora

Department of Pure and Applied Mathematics, Jomo Kenyatta University of Agriculture and Technology, Nairobi, Kenya

Email address:
douglasonchere44@gmail.com (Doglas Ambani Onchere), mathewkiny@jkuat.ac.ke (Mathew Ngugi Kinyanjui),
Prkiogora@fsc.jkuat.ac.ke (Phineas Roy Kiogora)
*Corresponding author

To cite this article:
Doglas Ambani Onchere, Mathew Ngugi Kinyanjui, Phineas Roy Kiogora. (2026). Study of Coupled Water-Sediment Energy Dynamics in Dam-Driven Closed-Conduit Flows. *Applied and Computational Mathematics, 15*(1), 1-12. https://doi.org/10.11648/j.acm.20261501.11

Received: 17 October 2025; **Accepted:** 27 October 2025; **Published:** 8 January 2026

Abstract: This study examines the coupled water-sediment energy dynamics in dam-driven closed-conduit flows, aiming to forecast discharge capacity and optimize release strategies for water supply, flood control, and hydropower generation. Sediment accumulation within dams significantly reduces hydraulic efficiency, limits the water supply, and undermines the overall benefits of dam operations by causing tunnel blockages, energy losses, and low discharge conditions. The novelty of this work is to develop a mathematical model that incorporates water-sediment interactions to accurately predict deposition zones, quantify energy dissipation, and support effective sediment management strategies. The governing equations are the continuity equation, the momentum equation, the energy equation, and the concentration equation. These equations are transformed from nonlinear partial differential equations into a system of linear ordinary differential equations using similarity transformations. The resulting equations are then solved using the collocation numerical technique and simulated in MATLAB software to obtain the profiles of the flow variables. The flow variables profiles are presented graphically. Flow parameters are varied, and their effects on the flow variables are discussed. It was observed that an increase in both the Reynolds number and the thermal Grashof number leads to an increase in velocity profiles, whereas an increase mass Grashof number produces an opposite effect by reducing the fluid velocity. Temperature of the fluid decreases with increasing Prandtl number, while an increase in the Eckert number leads to higher temperature profiles. The concentration profile decreases as the Schmidt number, Concentration ratio, and thermophoresis parameter increase. The research findings can help in making informed decisions on the in-dam safety, improving sediment management practices, ensuring reliable hydropower generation, and preventing blockage of the pipe. Furthermore, the research contributes to the design of more resilient discharge structures that can efficiently handle sediment, thereby extending the lifespan of hydraulic infrastructure and promoting sustainable operation of dam-driven systems.

Keywords: Dam Break, Sediment-laden Flow, Hydropower Plant, Sediment Deposition Rate, Non-Newtonian Fluid

1. Introduction

Dams play a vital role in water supply, irrigation, hydropower generation, and flood control, with many systems depending on closed-conduit tunnels to convey water from reservoirs to turbines and downstream consumers. However, sediment inflow and deposition pose a serious threat to long-term performance by reducing hydraulic efficiency, storage capacity, and discharge capability while increasing head losses, turbine abrasion, and maintenance demands. Globally, an estimated 0.5-1% of reservoir storage is lost each year to sedimentation, limiting operational reliability and reducing the economic and environmental benefits of dam infrastructure Chen et al [1]. In convergent pipes and penstocks, accelerated flow intensifies particle-fluid and particle wall interactions, leading to abrasion, secondary circulation, and localized deposition that disrupt velocity and pressure distributions. A clear understanding of sediment-laden flow in closed conduits is therefore essential for improving discharge capacity, minimizing erosion, and enhancing the efficiency and lifespan of dam operations. Hu et al [2] developed a simplified method to predict dam-breach hydrographs for various reservoir shapes. Peak discharge depends on initial water depth, while hydrograph shape is controlled by reservoir length. Analytical formulas were derived assuming instantaneous full dam failure. The approach provides a fast and reliable tool for dam-break flow assessment.

Omarova et al [3] studied dam-break water flow using a two-dimensional VOF-based model. The model solved Reynolds-averaged incompressible Navier-Stokes equations coupled with an interphase equation, using the $k-\epsilon$ turbulence closure. The VOF method accurately tracked free surface evolution while conserving mass. Simulation results were presented with contour plots and comparative graphs, capturing dynamic flow behavior. Model validation confirmed its reliability in reproducing experimental observations. The study demonstrates the model's potential for hazard assessment, emergency planning, and mitigation of dam-break impacts.

Zhou et al. [4] investigated the two-phase modeling of erosion and deposition during overtopping failures of landslide dams using GPU-accelerated ED-SPH. The study showed that soil deposition impedes eroded particles and reduces water velocity at the water-soil interface. Ignoring soil deposition, as in many existing models, leads to shorter breaching times and higher outburst flood discharges. The study further examined the re-erosion of deposited soils by varying the re-erosion coefficient, finding that lower coefficients result in higher peak discharges and reduced residual dam heights due to blockage by the deposited material.

Flood-driven suspended sediment transport across dilute to hyper-concentrated flows was investigated by Pu et al. [5]. A parameterized approach incorporating sediment size, Rouse number, mean concentration, and flow depth was employed to model the sediment concentration profile. The method demonstrated high accuracy in predicting profiles across a broad spectrum of sediment concentrations. Comparisons with measured data and existing models show that the approach reproduces dilute flow profiles with strong agreement. For hyper-concentrated flows, the measured data indicate a distinct separation between lower bed-load and upper suspended-load layers. The proposed model successfully identifies the transition point between these layers, providing a reliable tool for evaluating sediment distribution and transport dynamics in extreme flood events.

Wallwork et al. [6] conducted a review of mathematical models for suspended sediment transport. The study examined the influence of sediment particle size, flow depth, and velocity, alongside the roles of eddy viscosity and Rouse number on particle drag. It was emphasized that a critical threshold velocity is necessary to increase sediment concentration above the wash load. Additionally, the review explored the bursting phenomenon, describing how sediment can be entrained into the flow even at low mean velocities, highlighting the importance of intermittent turbulence in initiating sediment transport.

Pavlenko et al. [7] investigated enhancements to the mathematical modeling of the sedimentation process. The study incorporated the fractional nature of the Basset force, representing the Riemann-Liouville fractional integral as a Grunwald-Letnikov derivative. Consequently, an analytical general solution of the resulting fractional-order differential equation was obtained. The solution's validity within the real number range was rigorously established theoretically. Validation was performed through a specific analytical case study, and numerical confirmation was achieved using the S-approximation method in combination with the block-pulse operational matrix, demonstrating the model's accuracy and reliability. Mwangi et al [8] studied the maximum discharge of lateral pipes in sewage flow, examining how design parameters affect the flow capacity of lateral sewer pipes. The main objective of the study was to determine how pipe diameter, slope, effective inflow, and distance between manholes influence the maximum discharge achievable in sewer networks.

Maranzoni and Tomirotti et al. [9] reviewed three-dimensional numerical modeling of real-field dam-break flows. The study examined governing equations and numerical methods, emphasizing recent improvements in computational efficiency, modeling accuracy, and numerical techniques. Key dam-break case studies used for model validation were presented. The review provides guidance for researchers and modelers on recent developments in three-dimensional hydrodynamic models, helping to inform and direct future investigations on dam-break flows over complex real-world topography.

Li et al. [10] conducted an experimental study on sediment transport and sorting in pressurized pipes. The results indicated that sediment presence notably altered the flow velocity distribution. At the same flow rate, regions with high sediment concentration in the lower water layer experienced reduced velocity, whereas the upper layer velocity increased. Under low flow rates, higher sediment concentrations led to asymmetric cross-sectional velocity distributions. The vertical sediment concentration decreased with height, and clear stratification of sediment particles along the vertical direction was observed.

This study builds on Jiang et al [11], which modeled two-dimensional dam-break flows interacting with downstream structures using a VOF-based approach. Their work showed how obstacles and slope affect flow patterns, including diffraction, reflection, and viscous dissipation, but only considered water flow, omitting sediment transport, which is critical in real dam failures. The present research incorporates coupled water-sediment dynamics, focusing on entrainment, transport, and deposition, particularly in hydropower penstocks and downstream channels. Previous studies explored sediment transport in open channels and reservoirs, addressing shear stress, entrainment thresholds, and siltation, but closed-conduit systems like penstocks and spillways are less studied. In these confined, pressurized conduits, water and sediment are often treated separately, overlooking coupled energy effects that govern deposition and energy loss. This study investigates water-sediment-energy interactions in dam-driven convergent conduits to map deposition zones, quantify energy dissipation, and guide sediment management and flood mitigation in hydropower systems.

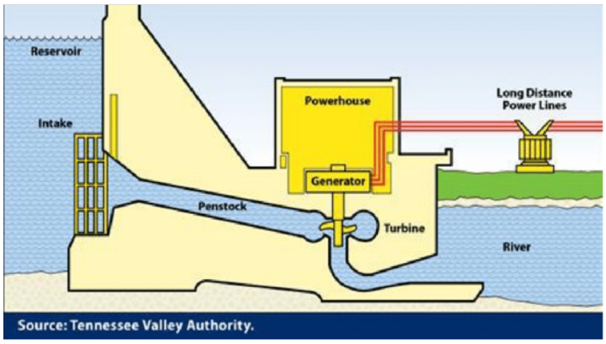

Figure 1. A schematic diagram of hydropower plant.

2. Mathematical Formulation

Unsteady, laminar, and two-dimensional flow of sediment-laden water through a tilted convergent conduit representative of a penstock or tunnel section is considered, as shown in Figure 2. At time $t = 0$, sediment-laden water of uniform concentration C_∞ and temperature T_∞ is introduced at the conduit inlet. The fluid exhibits motion exclusively in the radial direction and satisfies the no-slip condition. The inner wall of the conduit is assumed to be smooth, rigid, and impermeable, maintained at a constant wall temperature T_w. The tilted (α) and convergent geometry of the conduit significantly influence the hydrodynamic behavior, where sediment transport and deposition are governed by the combined effects of buoyancy, drag, diffusion, and gravitational settling under unsteady flow conditions.

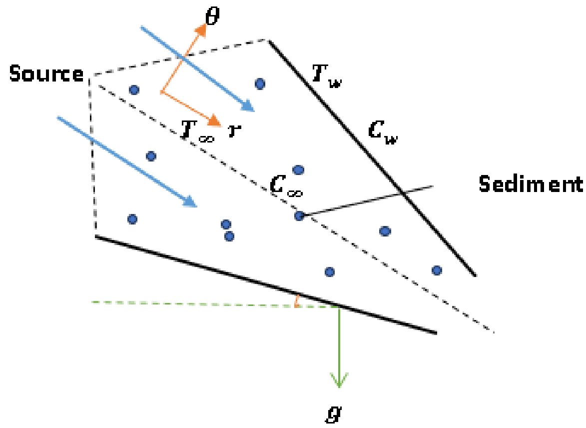

Figure 2. Computational Domain.

2.1. Governing Equations

The fundamental equations governing the fluid flow are the equation of continuity, the momentum equations, and the energy equation and the concentration equation.

2.1.1. Equation of Continuity

$$\frac{\partial \rho}{\partial t} + \frac{1}{r}\frac{\partial(\rho r u_r)}{\partial r} + \frac{1}{r}\frac{\partial(\rho u_\theta)}{\partial \theta} + \frac{\partial(\rho u_z)}{\partial z} = 0 \tag{1}$$

From the assumptions presented, the equation of continuity (1) reduces to:

$$\frac{1}{r}\frac{\partial(r u_r)}{\partial r} = 0 \tag{2}$$

Continuity Equation is used to satisfy any possible fluid flow.

2.1.2. Equation of Conservation of Momentum Along $\hat{r}$

$$\rho\left(\frac{\partial u_r}{\partial t} + u_r\frac{\partial u_r}{\partial r} + \frac{u_\theta}{r}\frac{\partial u_r}{\partial \theta} + u_z\frac{\partial u_r}{\partial z} - \frac{u_\theta^2}{r}\right) = -\frac{\partial p}{\partial r} + \mu\left[\frac{1}{r}\frac{\partial}{\partial r}\left(r\frac{\partial u_r}{\partial r}\right) + \frac{1}{r^2}\frac{\partial^2 u_r}{\partial \theta^2} + \frac{\partial^2 u_r}{\partial z^2}\right]$$
$$-\mu\left[\frac{2}{r^2}\frac{\partial u_\theta}{\partial \theta} + \frac{u_r}{r^2}\right] + F_B + F_D \tag{3}$$

2.1.3. Equation of Conservation of Momentum Along $\hat{\theta}$

$$\rho\left(\frac{\partial u_\theta}{\partial t} + u_r\frac{\partial u_\theta}{\partial r} + \frac{u_\theta}{r}\frac{\partial u_\theta}{\partial \theta} + u_z\frac{\partial u_\theta}{\partial z} - \frac{u_r u_\theta}{r}\right) = -\frac{1}{r}\frac{\partial p}{\partial \theta} + \mu\left[\frac{1}{r}\frac{\partial}{\partial r}\left(r\frac{\partial u_\theta}{\partial r}\right) + \frac{1}{r^2}\frac{\partial^2 u_\theta}{\partial \theta^2} + \frac{\partial^2 u_\theta}{\partial z^2}\right]$$
$$+\mu\left[\frac{2}{r^2}\frac{\partial u_r}{\partial \theta} - \frac{u_\theta}{r^2}\right] + F_B + F_D \tag{4}$$

Using Boussinesq approximation where $\rho(T,C)$, then $F_B = (\rho(T,C))g_r$. The buoyancy force depends on temperature and concentration. Then, the flow is caused by natural convection, and the convergent conduit is tilted at an angle α, but the gravitation force affects the flow along the radial direction.

$$g_r = \rho g cos\alpha \tag{5}$$

By Jean and Fan et al [12] defined a buoyancy force as: $\frac{F_B}{g_r} = \Delta\rho$. Then Lake and Thomas et al [13] defined volume expansion coefficient β as a function of ρ and Temperature.

$$F_B = g_r\beta(T - T_\infty)(cos\alpha) \tag{6}$$

Similarly, the buoyancy force due to concentration can be written as:

$$F_B = g_r\beta(C - C_\infty)(cos\alpha) \tag{7}$$

The drag force is the resistive force exerted by a fluid (liquid or gas) on a solid body moving relative to it. It acts opposite to the direction of motion. According to Stokes et al [14] derived the drag force (Creeping-flow) is:

$$F_D = B_d(u - u_p) \tag{8}$$

Since the flow is in two-dimensional (r,θ) and exhibits motion exclusively in the radial direction (that is, $u_\theta = 0$ and $u_z = 0$), the momentum equation along $\hat{r}$ reduces to:

$$\rho\left(\frac{\partial u_r}{\partial t} + u_r\frac{\partial u_r}{\partial r}\right) = -\frac{\partial p}{\partial r} + \mu\left[\frac{1}{r}\frac{\partial}{\partial r}\left(r\frac{\partial u_r}{\partial r}\right) + \frac{1}{r^2}\frac{\partial^2 u_r}{\partial \theta^2} - \frac{u_r}{r^2}\right] + g_r\beta(T-T_\infty)(cos\alpha) + g_r\beta(C-C_\infty)(cos\alpha) - B_d\left(u_r - u_{pr}\right) \tag{9}$$

Similary, equation of motion along $\hat{\theta}$ reduces to:

$$0 = -\frac{1}{\rho}\left(\frac{1}{r}\frac{\partial p}{\partial \theta}\right) + \frac{\mu}{\rho}\left(\frac{2}{r^2}\frac{\partial u_r}{\partial \theta}\right) + \frac{g_\theta\beta}{\rho}(T-T_\infty)(sin\alpha) + \frac{g_\theta\beta}{\rho}(C-C_\infty)(sin\alpha) \tag{10}$$

Eliminating the pressure term p, by differentiating equation (9) with respect to θ and equation (10) with respect to r, and equating them, we get the equation of motion whose motion is exclusively in the radial direction as:

$$\left[\frac{\partial^2 u_r}{\partial\theta\partial t}\right] = \frac{\mu}{\rho}\left[\frac{1}{r^2}\frac{\partial^3 u_r}{\partial\theta^3} + \frac{2}{r^2}\frac{\partial u_r}{\partial\theta} - \frac{2}{r}\frac{\partial^2 u_r}{\partial r\partial\theta}\right] - \frac{\partial u_r}{\partial\theta}\frac{\partial u_r}{\partial r} - u_r\frac{\partial^2 u_r}{\partial\theta\partial r} + \frac{g_r\beta}{\rho}(T-T_\infty)\left(\frac{\partial}{\partial\theta}\right)(cos\alpha) + \frac{g_r\beta}{\rho}(C-C_\infty)$$
$$\left(\frac{\partial}{\partial\theta}\right)(cos\alpha) - \frac{B_d}{\rho}\left(\frac{\partial}{\partial\theta}\right)(u_r - u_{pr}) - \frac{\beta g_\theta}{\rho}\left[(T-T_\infty) + \frac{\partial}{\partial r}(T-T_\infty)r\right] - \frac{\beta g_\theta}{\rho}\left[(C-C_\infty) + \frac{\partial}{\partial r}(C-C_\infty)r\right] \tag{11}$$

2.1.4. Equation of Energy

$$\rho c_p\left[\frac{\partial T}{\partial t} + u_r\frac{\partial T}{\partial r} + \frac{u_\theta}{r}\frac{\partial T}{\partial\theta} + u_z\frac{\partial T}{\partial z}\right] = k_f\left[\frac{1}{r}\frac{\partial}{\partial r}\left(r\frac{\partial T}{\partial r}\right) + \frac{1}{r^2}\frac{\partial^2 T}{\partial\theta^2} + \frac{\partial^2 T}{\partial z^2}\right] +$$
$$2\mu\left[\left(\frac{\partial u_r}{\partial r}\right)^2 + \left(\frac{1}{r}\frac{\partial u\theta}{\partial\theta} + \frac{u_r}{r}\right)^2 + \left(\frac{\partial u_z}{\partial z}\right)^2\right] + \mu\left[\left(\frac{1}{r}\frac{\partial u_r}{\partial\theta} + \frac{\partial u_\theta}{\partial r} - \frac{u_\theta}{r}\right)^2 + \left(\frac{\partial u_\theta}{\partial z} + \frac{1}{r}\frac{\partial u_z}{\partial\theta}\right)^2\right] \tag{12}$$

Since the fluid exhibits motion exclusively in the radial direction $u_\theta = 0$ and $u_z = 0$, and dividing through by ρc_p, and making $\frac{\partial T}{\partial t}$ the equation of energy (12) reduces to:

$$\frac{\partial T}{\partial t} = 2\frac{\mu}{\rho c_p}\left[\left(\frac{\partial u_r}{\partial r}\right)^2 + \left(\frac{u_r}{r}\right)^2\right] + \frac{\mu}{\rho c_p}\left[\frac{1}{r}\left(\frac{\partial u_r}{\partial\theta}\right)^2\right] + \frac{k_f}{\rho c_p}\left[\frac{1}{r}\frac{\partial}{\partial r}\left(r\frac{\partial T}{\partial r}\right)\frac{1}{r^2}\frac{\partial^2 T}{\partial\theta^2}\right] - u_r\frac{\partial T}{\partial r} \tag{13}$$

2.1.5. Concentration Equation

$$\frac{\partial C}{\partial t} + u_r\frac{\partial C}{\partial r} + \frac{u_r}{r}\frac{\partial C}{\partial\theta} + u_z\frac{\partial C}{\partial z} = D\left(\frac{1}{r}\frac{\partial}{\partial r}\left(r\frac{\partial C}{\partial r}\right) + \frac{1}{r^2}\frac{\partial^2 C}{\partial\theta^2} + \frac{\partial^2 C}{\partial z^2}\right) + \frac{1}{r}\frac{\partial}{\partial r}(ru_{Tr}C) + \frac{1}{r}\frac{\partial}{\partial\theta}(u_{T\theta}C) + \frac{1}{r}\frac{\partial}{\partial z}(u_{Tz}C) - \Psi C \tag{14}$$

Where u_T is the thermophoresis term and Ψ is the correction factor for sediment deposition. Since the fluid exhibits motion exclusively in the radial direction, $u_\theta = 0$ and $u_z = 0$, then the equation of concentration (14) reduces to:

$$\frac{\partial C}{\partial t} + u_r\frac{\partial C}{\partial r} = D\left(\frac{1}{r}\frac{\partial C}{\partial r} + \frac{\partial^2 C}{\partial r^2} + \frac{1}{r^2}\frac{\partial^2 C}{\partial\theta^2}\right) + \frac{1}{r}\frac{\partial}{\partial\theta}(ru_{T\theta}C) - \Psi C \tag{15}$$

By Talbot et al [15] defined the thermophoretic velocity u_T as:;

$$u_T = -\frac{K_T}{T}\frac{\mu}{\rho}\frac{dT}{d\theta} \tag{16}$$

The sediment flow is a long θ, where $\frac{\partial C}{\partial r} = \frac{\partial^2 C}{\partial r^2} = 0$. The $\frac{\partial C}{\partial t}$is the radial temperature gradient, K_T thermophoretic coefficient, which ranges in value from 0.2 to 1.2 as indicated by Batchelor and Shen et al [16]. Substituting equation(16) into equation(15) becomes:

$$\frac{\partial C}{\partial t} - D\left(\frac{1}{r^2}\frac{\partial^2 C}{\partial \theta^2}\right) + \frac{\mu K_T}{\rho}\left[\frac{\partial^2 T}{\partial \theta^2}\frac{C}{T} - \frac{C}{T^2}\left(\frac{\partial T}{\partial \theta}\right)^2 + \frac{1}{T}\frac{\partial T}{\partial \theta}\frac{\partial C}{\partial \theta}\right] + \varPsi C = 0 \tag{17}$$

2.2. Similarity Transformation

Boundary condition proposed by Mavi and Chinyoka et al [17] is given by:
At the center where $\theta = 0$

$$u_r = u_\infty, u_\theta = 0, T = T_\infty, C = C_\infty \tag{18}$$

On the wall where $\theta = \pm\alpha$

$$u_r = 0, u_\theta = u_0, T = T_W, C = C_W \tag{19}$$

Where u_∞ is the velocity at the center and α represents the cone angle. The following similarity transformation is employed to convert the nonlinear partial differential equations into a system of nonlinear ordinary differential equations. Nagler et al [18], the similarity transformation for the velocity field is expressed as

$$u_r(r,\theta,t) = -\frac{Q}{r}\frac{1}{\sigma^{m+1}}F(\theta) \tag{20}$$

Similarly, the velocity of a particle (sediment) is given by:

$$u_{pr}(r,\theta,t) = -\frac{Q}{r}\frac{1}{\sigma^{m+1}}G(\theta) \tag{21}$$

Where Q denotes planar volumetric flow rate, m is a constant associated with the cone angle α, σ denotes the time-dependent length scale, and F represents the dimensionless velocity function. Sattar et al [19], similarity transformations for temperature and concentration are expressed as:

$$\frac{w(\theta)}{\sigma^{m+1}} = \frac{T - T_w}{T_\infty - T_w} \tag{22}$$

$$\frac{\phi(\theta)}{\sigma^{m+1}} = \frac{C - C_w}{C_\infty - C_w} \tag{23}$$

Applying the transformations (20), (21), (22), and (23) to equations (2), (11), (13), and (17) yields:

$$(m+1)\frac{\rho}{\mu}\frac{r^2}{\sigma^{m+1}}\frac{d\sigma}{dt}F'(\theta) = -F'''(\theta) - 4F'(\theta) - 2\frac{\rho}{\mu}\frac{Q}{\sigma^{m+1}}F(\theta)F'(\theta) + \frac{\beta r^3 g_r}{\mu Q}(T_\infty - T_w)w'(\theta) + \frac{\beta r^3 g_r}{\mu Q}$$
$$(C_\infty - C_w)\phi'(\theta) + \frac{18\Phi\mu r^2}{d_p^2\rho}\left(F'(\theta) - G'(\theta)\right) - \frac{\beta r^3 g_\theta}{\mu Q}(T_\infty - T_w)w(\theta) - \frac{\beta r^3 g_\theta}{\mu Q}(C_\infty - C_w)\phi(\theta) \tag{24}$$

$$\frac{k_f}{\rho C_P}w''(\theta) + \frac{(m+1)r^2}{\sigma^{m+1}}\frac{d\sigma}{dt}w(\theta) + \frac{\mu}{\rho c_p}\frac{Q^2}{r^2}\frac{1}{(T - T_\infty)\sigma^{m+1}}\left[4(F(\theta))^2 + \left(F'(\theta)\right)^2\right] = 0 \tag{25}$$

$$\frac{(m+1)}{\sigma^{m+1}}\frac{\rho}{\mu}\frac{d\sigma}{dt}r^2\phi(\theta) + \frac{\rho}{\mu}D\phi''(\theta) - r^2 K_T\left(\frac{\phi(\theta) + \frac{C_w}{C_\infty - C_W}\sigma^{m+1}}{w(\theta) + \frac{T_w}{T - T_w}\sigma^{m+1}}\right)w''(\theta) +$$
$$\frac{r^2 K_T}{w + \frac{T_w}{T - T_w}\sigma^{m+1}}\left[\left((\phi(\theta) + \frac{C_w}{C_\infty - C_W}\sigma^{m+1}\right)\right]\left[\frac{1}{w(\theta) + \frac{T_w}{T - T_w}\sigma^{m+1}}\right]\left(w'(\theta)\right)^2 -$$
$$r^2 K_T\left(\frac{1}{w(\theta) + \frac{T_w}{T - T_w}\sigma^{m+1}}\right)w'(\theta)\phi'(\theta) - \frac{\rho\Psi}{\mu r^2}\left[\phi(\theta) + \frac{C_w}{C_\infty - C_w}\sigma^{m+1}\right] = 0 \tag{26}$$

The given non-dimensional parameters are observed from equations 24-26: Reynolds number: $Re = \frac{Q\rho}{\mu}$, Unsteadiness parameter: $\lambda = \frac{\rho}{\mu}\frac{d\sigma}{dt}$, Mass Grashof number: $Gr_{(C)} = \frac{\beta r^3 g_r}{\mu}\left(C_\infty - C_w\right)$, Thermal Grashof number: $Gr_{(T)} = \frac{\beta r^3 g_r}{\mu}\left(T_\infty - T_w\right)$, Drag parameter: $K_d = \frac{18\Phi\mu r^2}{d_p^2\rho}$, Prandtl number: $Pr = \frac{\mu c_p}{k_f}$, Eckert number: $Ec = \frac{Q^2}{c_p(T-T_\infty)}$, Schmidt number: $Sc = \frac{\rho}{\mu}D$, Thermophoresis parameter: $Nt = \frac{T_w}{T-T_w}$, Concentration ratio: $Nc = \frac{C_w}{C_\infty - C_w}$

Then, substituting the dimensionless parameters into equations 24, 25, and 26 yielded:

$$(m+1)\frac{\lambda r^2}{\sigma}F'(\theta) + F'''(\theta) + 4F'(\theta) + 2\frac{Re}{\sigma^{m+1}}F(\theta)F'(\theta) - \frac{Gr_{(T)}}{Q}w'(\theta) - \frac{Gr_{(C)}}{Q}\phi'(\theta) + K_d\left(F'(\theta) - G'(\theta)\right) + \frac{Gr_{(T)}}{Q}w(\theta) + \frac{Gr_{(C)}}{Q}\phi(\theta) = 0 \tag{27}$$

$$\frac{1}{Pr}w''(\theta) + \frac{(m+1)}{\sigma^{m+1}}r^2\lambda w(\theta) + \frac{Ec}{r^2\sigma^{m+1}}\left[4\left(F(\theta)\right)^2 + \left(F'(\theta)\right)^2\right] = 0 \tag{28}$$

$$\frac{(m+1)}{\sigma^{m+1}}\lambda r^2\phi(\theta) + \frac{1}{S_c}\phi''(\theta) - \left(\frac{r^2K_T\left(\phi(\theta) + N_c\sigma^{m+1}\right)}{w(\theta) + N_t\sigma^{m+1}}\right)w''(\theta) + \frac{r^2K_T}{w(\theta) + N_t\sigma^{m+1}}\left[\left(\phi(\theta) + N_c\sigma^{m+1}\right)\frac{1}{w(\theta) + N_t\sigma^{m+1}}\right] \left(w'(\theta)\right)^2 - \left(\frac{r^2K_T}{w(\theta) + N_t\sigma^{m+1}}\right)w'(\theta)\phi'(\theta) - \frac{\rho\Psi}{\mu r^2}\left[\phi(\theta) + N_c\sigma^{m+1}\right] = 0 \tag{29}$$

Similarly, transform the boundary conditions with the transformations 20, 22, and 23 to obtain:
At the center $\theta = 0$

$$F(0) = 1, F'(0) = 0, w(0) = \sigma^{m+1}, \phi(0) = 0 \tag{30}$$

On the wall $\theta = \pm\alpha$

$$F(\alpha) = 0, w(\alpha) = 0, \phi(\alpha) = \sigma^{m+1} \tag{31}$$

3. Spectral Collocation

The collocation method is a powerful numerical technique for solving boundary value problems (BVPs) by approximating the solutions of ordinary differential equations (ODEs) with suitable polynomial basis functions. It is widely applied to both ordinary and partial differential equations within a specified domain. The method is known to be convergent, consistent, and stable, three essential properties that ensure reliability when selecting an appropriate numerical scheme for model analysis.

In this study, the governing higher-order nonlinear ODEs are first reduced to an equivalent system of first-order nonlinear equations. The following substitutions are introduced:

$$y_1 = F, y_2 = F', y_3 = F'', y_4 = w, y_5 = w', \quad y_6 = \phi, y_7 = \phi' y_8 = G, y_9 = G' \tag{32}$$

Applying these conventions, equations (32) to equations (27), (28), and (29), the equations are transformed into a first-order system. The resulting system of first-order equations can be expressed in matrix form as follows:

$$\begin{bmatrix} y_1' \\ y_2' \\ y_3' \\ y_4' \\ y_5' \\ y_6' \\ y_7' \end{bmatrix} = \begin{bmatrix} y_2 \\ y_3 \\ -(m+1)\frac{\lambda r^2}{\sigma}y_2 - 4y_2 - 2\frac{Re}{\sigma^{m+1}}y_1y_2 + \frac{Gr_{(T)}}{Q}y_5 + \frac{Gr_{(C)}}{Q}y_7 - \frac{Gr_{(T)}}{Q}y_4 - \frac{Gr_{(C)}}{Q}y_6 + K_d\left(y_2 - y_9\right) \\ y_5 \\ -P_r\frac{(m+1)}{\sigma^{m+1}}r^2\lambda y_4 - \frac{P_rEc}{r^2\sigma^{m+1}}\left[4\left((y_1)^2 + (y_2)^2\right)\right] \\ y_7 \\ \frac{-(m+1)r^2}{\sigma^{m+1}}\lambda y_6S_c + \left(\frac{r^2K_TS_c\left(y_6 + N_c\sigma^{m+1}\right)}{y_4 + N_t\sigma^{m+1}}\right)y_5 - \left(\frac{r^2K_T}{y_4 + N_t\sigma^{m+1}}\right)\left[y_5y_7 - \frac{\left(y_6 + N_c\sigma^{m+1}\right)}{\left(y_4 + N_t\sigma^{m+1}\right)}(y_5)^2\right] + \frac{\rho\Psi}{\mu r^2}\left[y_6 + N_c\sigma^{m+1}\right] \end{bmatrix} \tag{33}$$

The boundary conditions 30 and 31 are subjected to conventions (32) to be reduced into first order:
At the center $\theta = 0$

$$y_1(0) = 1, y_2(0) = 0, y_4(0) = \sigma^{m+1}, y_6(0) = 0 \tag{34}$$

On the wall $\theta = \pm\alpha$

$$y_2(\alpha) = 0, y_4(\alpha) = 0, y_6(\alpha) = \sigma^{m+1} \tag{35}$$

4. Results and Discussion

The systems of matrix equation (33) together with the boundary conditions (34) and (35) were implemented in BVP4c, an inbuilt function in MATLAB, and the results were visualized through graphs. These graphical representations are comprehensively discussed as follows:

4.1. Effects of Flow Parameters on Velocity

From figure 3, it can be observed that an increase in the Reynolds number results in higher radial velocity profiles within the convergent pipe under laminar flow conditions. The Reynolds number represents the ratio of inertial forces to viscous forces in a fluid. As this ratio increases, viscous effects weaken relative to inertia, allowing the fluid to move with less resistance and therefore attain higher velocities. Conversely, when the Reynolds number decreases, viscous forces dominate the flow, increasing resistance and consequently reducing the fluid velocity.

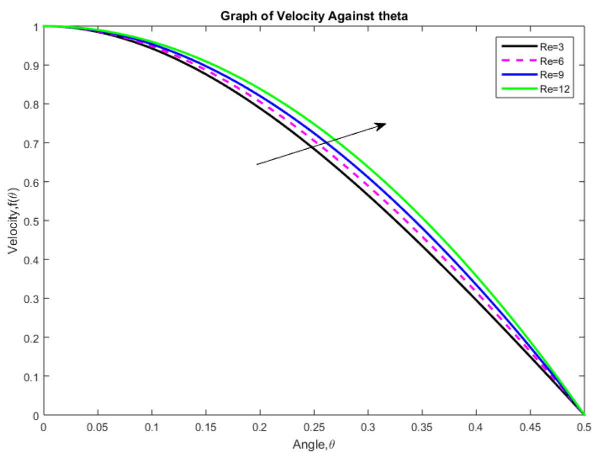

Figure 3. *Effect of varying Reynolds' number on velocity profile.*

From Figure 4, it can be observed that an increase in the unsteadiness parameter results in a noticeable reduction in fluid velocity. A larger unsteadiness parameter signifies stronger temporal variations in the flow, typically arising from time-dependent boundary conditions, oscillatory inflow, or other transient effects. Under such conditions, fluid particles are compelled to continuously readjust to the rapidly changing flow environment. This persistent adjustment introduces inertial resistance, which restricts the fluid's ability to accelerate or sustain higher velocities. Consequently, the overall velocity of the flow diminishes as the level of unsteadiness intensifies.

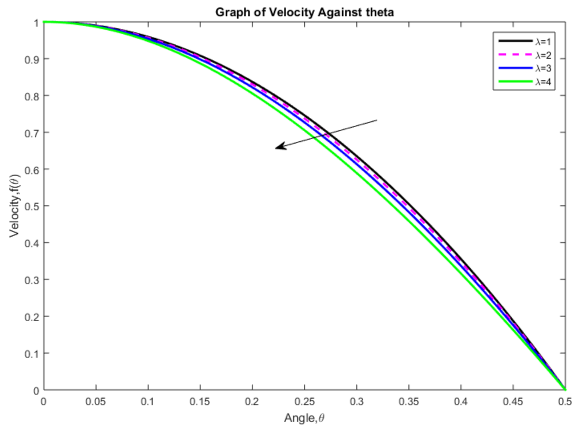

Figure 4. *Effect of varying unsteadiness parameter on velocity profile.*

From Figure 5, it can be observed that an increase in the mass Grasshof number $Gr_{(C)}$ results in a decrease in the velocity of the fluid flow. The mass Grasshof number is defined as the ratio of buoyancy forces to viscous forces. An increase in the value of mass Grasshof number $Gr_{(C)}$ implies an increase in the concentration difference i.e. $(C_f - C_w)$ This means that the concentration of sediment particles at the wall C_∞ is increasing compared to that of the radial. This results in to decrease in the concentration of sediment particles moving towards the radial. The relative velocity between the fluid and the sediment particles increases towards the wall, resulting in a decreased velocity of fluid flow.

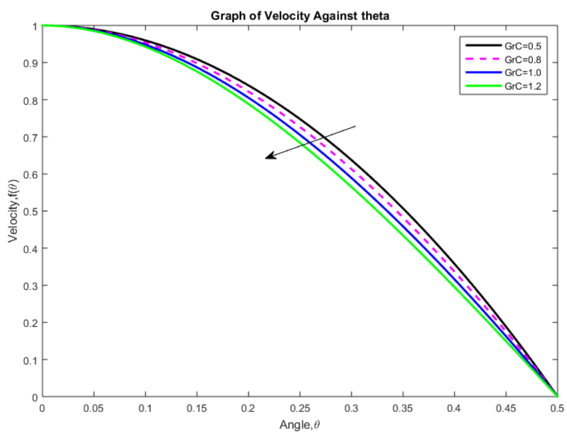

Figure 5. *Effect of varying Mass Grashof number on velocity profile.*

From Figure 6, it can be observed that an increase in the thermal Grashof number $Gr_{(T)}$ results in an increase in the velocity of the flow. The thermal Grashof number is defined as the ratio of buoyancy forces to viscous forces. Implies that an increase in $Gr_{(T)}$ leads to increased forces that are driving the fluid flow. This implies increased velocity of the fluid flow. An increase in $Gr_{(T)}$ also implies an increase in the fluid temperature. This implies that the fluid is becoming less viscous, thereby increasing its ability to flow. This results in increased velocity of the fluid. An increase in fluid temperature further implies a decrease in sediment particles, which implies a decrease in relative velocity between the sediment particles and the fluid. A decrease in relative velocity implies an increase in the velocity of fluid flow.

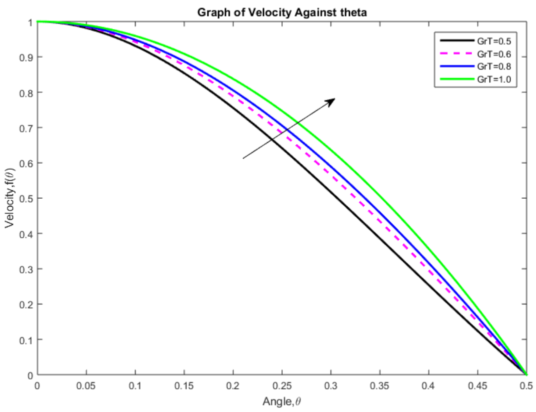

Figure 6. *Effect of varying Thermal Grashof number on velocity profile.*

From figure 7, it can be observed that as the Drag parameter increases, the fluid velocity decreases significantly across the angular domain. This trend highlights the role of drag in transferring momentum from the carrier fluid to the suspended sediments, thereby enhancing energy dissipation. Physically, higher sediment concentration or smaller particle size (increasing the Drag parameter) amplifies this drag effect, resulting in stronger water-sediment coupling and reduced fluid motion. Such behavior is crucial in predicting regions of flow retardation, energy loss, and potential sediment deposition in hydraulic systems.

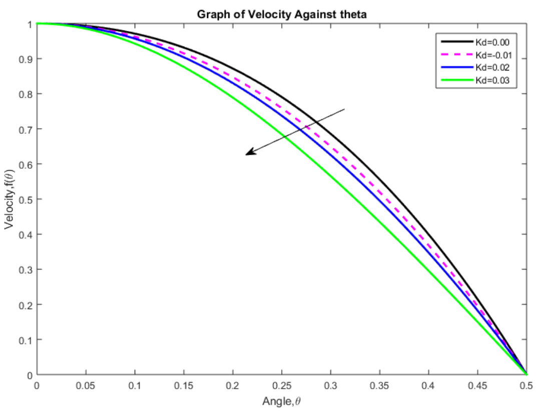

Figure 7. *Effect of varying Drag parameter number on velocity profile.*

4.2. Effects of Flow Parameters on Temperature

From Figure 8, it can be observed that an increase in the Prandtl number leads to a reduction in the temperature of the sediment-laden fluid. The Prandtl number represents the ratio of momentum diffusivity to thermal diffusivity. Thus, a higher Prandtl number corresponds to stronger viscous effects and weaker thermal diffusivity. As a result, heat diffuses more slowly through the fluid layer, reducing the rate of thermal transport. This slower heat propagation causes the sediment-laden fluid to exhibit lower temperature distributions.

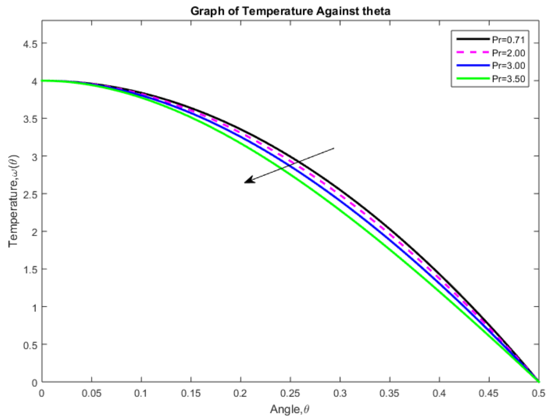

Figure 8. *Effect of varying Prandtl number on Temperature profile.*

From Figure 9, it is observed that an increase in the Eckert number Ec leads to increased temperature fluid flow. The Eckert number quantifies the relative contribution of kinetic energy to internal thermal energy within a fluid flow. An increase in the Eckert number implies a decrease in the temperature difference $T_f - T_w$. This shows that the center temperature is decreasing in comparison to the wall temperature, which is increasing. This implies balancing of temperature as a result of convection curren,t leading to minimal increase in temperatureAn increasese in Ec also implies, kinetic energy is predominant,, and thu,s there is a lot of bombardment of the fluid particles and hence causing a lot of vibration of the fluid particles and consequently an increment of velocity of the fluid since even viscous forces are not predominant.

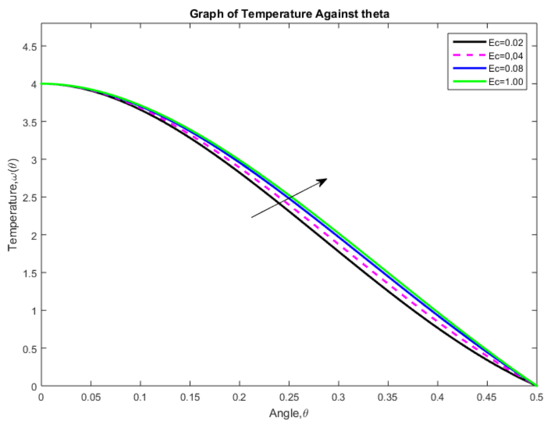

Figure 9. *Effect of varying Eckert number on Temperature profile.*

4.3. Effects of Flow Parameters on Concentration

From Figure 10, it is observed that an increase in the Schmidt number results in a reduction in the concentration of the sediment-laden flow. The Schmidt number expresses the ratio of momentum diffusivity to mass diffusivity, and therefore, a larger value indicates that molecular mass diffusion is relatively weak compared to momentum diffusion. When mass diffusivity is small, the transport and mixing of sediment become less effective, leading to lower concentration levels within the fluid. For cases where $Sc < 1$, mass diffusion dominates momentum diffusion, allowing rapid spreading of the transported species while viscous effects play a minor role. This behavior influences the coupled water-sediment transport mechanisms by altering the balance between viscous motion and molecular diffusion, ultimately controlling sediment redistribution and the associated energy dissipation within the flow system.

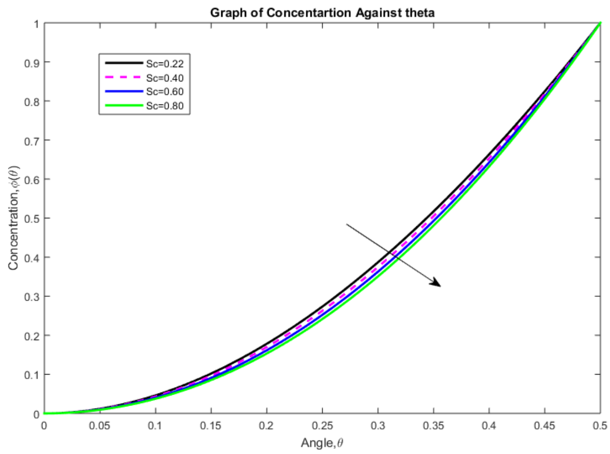

Figure 10. *Effect of varying Schmidt number on concentration profile.*

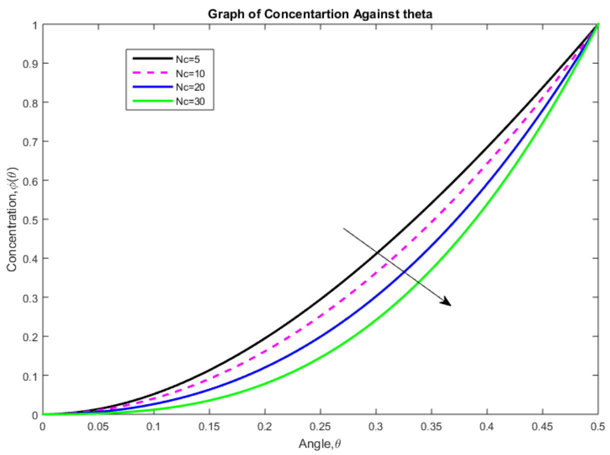

Figure 11. *Effect of varying Concentration ratio on concentration profile.*

From Figure 11, it is observed that an increase in the concentration ratio Nc results in a decrease in the concentration of sediment particles. By definition, an increase in the concentration ratio (Nc) implies a decrease in the concentration difference $C_f - C_w$. This implies that the concentration of sediment particles at the walls is decreasing as the radius increases. This implies that the particles are moving towards the radial. Increasing Nc reduces the concentration profile, implying enhanced sediment diffusion and stronger particle-fluid interaction. Physically, this corresponds to more efficient sediment transport in dam-driven flows, where higher Nc promotes faster dispersion and reduces particle accumulation. This behavior directly influences the coupled water-sediment energy dynamics by altering the viscous dissipation and drag forces within the conduit.

From Figure 12, it is observed that an increase in the thermophoresis parameter causes sediment particles to migrate away from regions of higher temperature, resulting in a lowered concentration within the fluid. By definition, the thermophoresis parameter Nt implies a decrease in the temperature difference $T_f - T_w$. This means that the wall temperature T_w is increasing, implying that the sediment particles are becoming soluble. This results in a decrease in the concentration of sediment particles. Physically, this reflects the coupling between thermal energy and sediment transport: higher thermophoresis accelerates sediment dispersion, reduces the overall particle concentration in the core flow, and promotes deposition along conduit boundaries. Consequently, the thermophoretic effect plays a significant role in modifying the coupled water-sediment energy dynamics by intensifying particle fluid interaction and altering the flow resistance in dam-driven conduit systems.

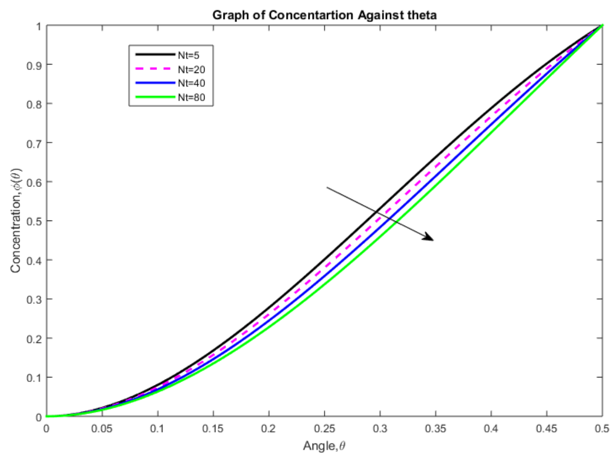

Figure 12. *Effect of varying Thermophoresis parameter on concentration profile.*

From Figure 13, it is observed that an increase in ψ leads to a decrease in the concentration of sediment particles. The methods of preventing sediment deposition are assigned different rank values, which can be represented by ψ, where ψ represents the correction factor for sediment concentration. The first and most used rank in preventing sediment deposition in hydropower tunnels and penstocks is flushing or sluicing, which uses high-velocity flows to scour and transport sediments downstream, giving it the highest correction factor ψ. The second rank is settling basins or desilting chambers, which reduce velocity and allow particles to settle before entering the system. The third rank is sediment bypass tunnels, which divert high-sediment flows. The fourth rank is hydraulic design optimization, ensuring self-cleansing velocities and smooth linings to minimize deposition.

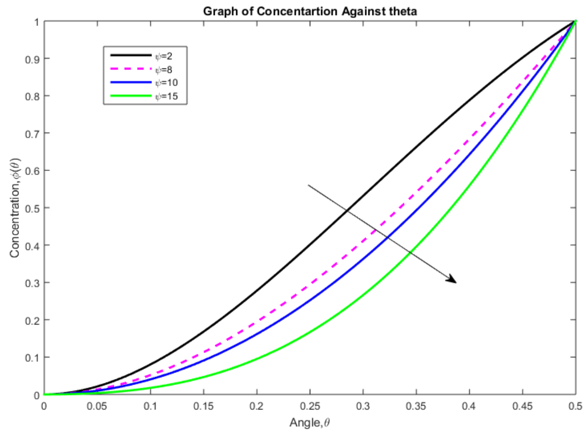

Figure 13. *Effect of varying correction factor on concentration profile.*

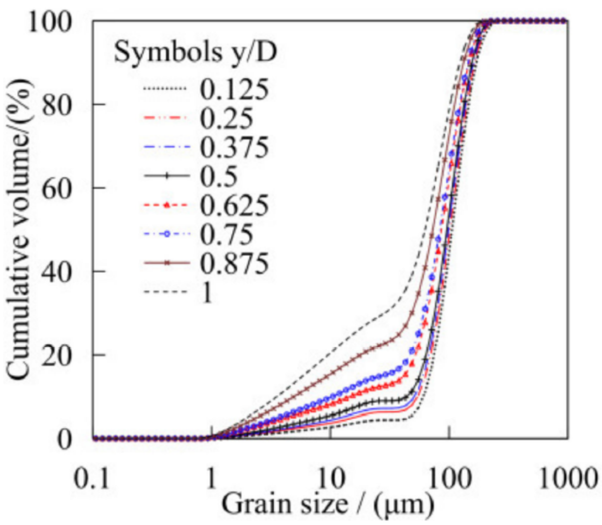

(a) Li et al [10] Concentration profile.

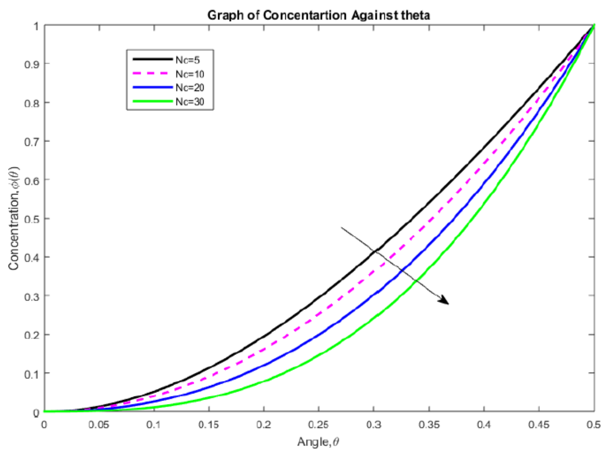

(b) Concentration profile for sediment-laden flow.

Figure 14. *Graphs of Concentration profiles in Li et al [10] and in the Present Study.*

5. Validation of Results

Comparison with the experimental study by Li et al. [10] on sediment transport and particle sorting in pressurized pipes reveals similar trends to the present study. In solid-liquid two-phase flows under natural conditions, particle movement and deposition are often accompanied by segregation, resulting in non-uniform distributions. Notably, sediment concentration tends to be higher near the pipe walls compared to the central region. The temporal and spatial distribution of these particles provides valuable insights into environmental changes, geomorphic evolution, and the dynamics of solid-liquid flows. Figure 14 presents a direct comparison of the observed patterns.

6. Conclusions

This study examined the coupled water-sediment energy dynamics in a dam-driven closed-conduit flow. The governing equations were formulated from the principles of continuity, momentum conservation, energy, and concentration equation (mass transport). The effects of the relevant non-dimensional parameters on the flow variables were analyzed in detail. Based on the findings, the following conclusions can be drawn:

1. Increase in Reynolds' number leads to an increase in velocity profiles.
2. An Increase in the unsteadiness parameter leads to a decrease in the flow velocity in velocity profiles.
3. Both thermal Grashof number and mass Grashof number affect the fluid velocity. The thermal Grashof number increases the velocity of the fluid flow, while the Grashof number decreases the velocity of the fluid flow.
4. An Increase in the Drag parameter leads to a decrease in the flow velocity in velocity profiles.
5. Increase in Prandtl number leads to a decrease of temperature; similarly, an increase in Eckert number leads to an increase the temperature.
6. Increase in Schmidt number implies decrease in mass diffusivity of the sediment particles, which also implies decreased movement of these sediment particles, resulting in decreased concentration.
7. Increase in Concentration ratio implies a decrease in concentration of the sediment particles in the fluid. This implies that the particles are moving towards the radial
8. Increasing the Thermophoresis parameter implies an increase in T_w, which implies that particles are moving to the center and thus will be decreasing towards the wall of the cylindrical conduit.
9. As the parameter ψ increases, the concentration of sediment deposition decreases due to reduced particle accumulation within the flow.

7. Recommendations

The main users of this study are the Dam, irrigation, and power plant engineers. Recommendations to the user are as follows:

1. Sensor technology using transmitters to determine levels of growth of sediment particles can be used to relay information to the dam operator and the power plant engineers before carrying out the work during operations.
2. Incorporate temperature variation monitoring (viscous dissipation and thermophoresis) into dam operation to improve prediction of flow resistance and sediment transport
3. Convergent points should be avoided where possible because they are prone to deposits of materials. They have high friction between the sediment-laden fluid and the walls of the spillways or penstock ppipesresulting in corrosion in the penstock pipes.
4. Apply the developed coupled water-sediment energy model in dam management systems to forecast sediment deposition zones and optimize discharge strategies.

The recommendations for further research are as follows:

1. Use of a compressible fluid.
2. Consider a turbulent or a transitional fluid flow.
3. Study of multi-phase fluid flow.
4. Use of a different numerical technique.
5. Use of a slip interface.

ORCID

0009-0004-9534-948X (Doglas Ambani Onchere)

Nomenclature

C_p	Specific Heat Capacity
u, v, w	Velocity Components
t	Time
p	Pressure
T	Temperature
C	Concentration of the Fluid
F	Body Forces
$gr; g\theta; gz$	Gravitational Force of the Fluid
U_r, U_θ, U_Z	Velocity Components
ρ	Fluid Density
K	Thermal Conductivity
k_f	Thermal Conductivity of the Fluid
ϕ	Viscous Dissipation
ψ	Correction Factor
F_B	Buoyancy Force
F_D	Drag Force
Bd	Drag Coefficient
x, y, z	Cartesian Coordinate System
r, θ, z	Cylindrical Coordinate System
Re	Reynolds Number
$G(C)$	Mass Grashof Number
$G(T)$	Thermal Grashof Number
Kd	Drag Parameter
Pr	Prandtl
E_c	Eckert Number
N_c	Concentration Ratio
N_t	Thermophoresis Parameter
S_c	Schmidt Number
∇	Gradient Operator

Abbreviations

PDEs	Partial Differential Equations
ODE	Ordinary Differential Equations
CFD	Computational Fluid Dynamics
MATLAB	Matrix Laboratory
BVP	Boundary Value Problem
BVP4C	Boundary Value Problem 4^{th} Order Collocation
HAM	Homotopy Analysis Method
IVP	Initial Value Problem

Author Contributions

Doglas Ambani Onchere: Conceptualization, Data curation, Formal Analysis, Funding acquisition, Investigation, Methodology, Project administration, Resources, Software, Visualization, Writing - original draft, Writing - review editing

Mathew Ngugi Kinyanjui: Supervision, Validation

Phineas Roy Kiogora: Supervision, Validation

Conflicts of Interest

The authors declare no conflicts of interest regarding the publication of this research article.

References

[1] Lu Chen, Bingqi Hou, Ting Zhan, Linsong Ge,Yehongping Qin, and Wenjie Zhong. Water-sediment energy joint operation model of large-scale reservoirgroup for sediment-laden rivers. Journal of CleanerProduction, 370: 133271, 2022.

[2] Hui Hu, Jianfeng Zhang, Tao Li, and Jie Yang. A simplified mathematical model for the dam-breach hydrograph for three reservoir geometries following asudden full dam break. Natural Hazards, 102: 1515-1540, 2020.

[3] Perizat Omarova, Timur Merembayev, and Yedilkhan Amirgaliyev. Mathematical modeling of water movement during a dam break using the vof method. Scientific Journal of Astana IT University, 14: 14, 2023.

[4] Mingjun Zhou, Zhenming Shi, Chong Peng, Ming Peng, Kahlil Fredrick E Cui, Bo Li, Limin Zhang, and Gordon GD Zhou. Two-phase modelling of erosionand deposition process during overtopping failure oflandslide dams using gpu-accelerated ed-sph. Computersand Geotechnics, 166: 105944, 2024.

[5] Jaan H Pu, Joseph T Wallwork, Md Amir Khan, Manish Pandey, Hanif Pourshahbaz, Alfrendo Satyanaga, Prashanth R Hanmaiahgari, and Tim Gough. Flood suspended sediment transport: combined modelling from dilute to hyper-concentrated flow. Water, 13(3): 379, 2021.

[6] Joseph T Wallwork, Jaan H Pu, Snehasis Kundu, Prashanth R Hanmaiahgari, Manish Pandey, Alfrendo Satyanaga, Md Amir Khan, and Alastair Wood. Review of suspended sediment transport mathematical modelling studies. Fluids, 7(1): 23, 2022.

[7] Ivan Pavlenko, Marek Ochowiak, Praveen Agarwal, Radosław Olszewski, Bernard Michałek, and AndzelikaKrupiska. Improvement of mathematical model forsedimentation process. Energies, 14(15): 4561, 2021.

[8] Reuben Wambugu Mwangi, Mathew Ngugi Kinyanjui, and Phineas Roy Kiogora. Maximum discharge oflateral pipes in sewage flow. Applied and Computational Mathematics, 14(1): 1-11, 2025.

[9] Andrea Maranzoni and Massimo Tomirotti. Three dimensional numerical modelling of real-field dam-break flows: review and recent advances. Water, 15(17): 3130, 2023.

[10] Yan Li, Jinliang Zhang, Haijue Xu, and Yuchuan Bai. Experimental study on the characteristics of sediment transport and sorting in pressurized pipes. Water, 13(19): 2782, 2021.

[11] Haoyu Jiang, Bowen Zhao, Zhang Dapeng, and KeqiangZhu. Numerical simulation of two-dimensional dam failure and free-side deformation flow studies. Water, 15(8): 1515, 2023.

[12] Rong-Her Jean and Liang-Shih Fan. On the model equations of gibilaro and foscolo with corrected buoyancy force. Powder technology, 72(3): 201-205, 1992.

[13] Graham J Lake and Allen G Thomas. The strengthof highly elastic materials. Proceedings of the RoyalSociety of London. Series A. Mathematical and Physical Sciences, 300(1460): 108-119, 1967.

[14] George Gabriel Stokes et al. On the effect of the internal friction of fluids on the motion of pendulums. 1851.

[15] LRKRWDR Talbot, Robert K Cheng, Robert W Schefer, and D Roger Willis. Thermophoresis of particles ina heated boundary layer. Journal of fluid mechanics, 101(4): 737-758, 1980.

[16] GK Batchelor and C Shen. Thermophoretic deposition of particles in gas flowing over cold surfaces. Journal of Colloid and Interface Science, 107(1): 21-37, 1985.

[17] Anele Mavi and Tiri Chinyoka. Finite volume computational analysis of the heat transfer characteristicin a double-cylinder counter-flow heat exchanger withviscoelastic fluids. In Defect and Diffusion Forum, volume 424, pages 19-43. Trans Tech Publ, 2023.

[18] J Nagler. Jeffery-hamel flow of non-newtonian fluidwith nonlinear viscosity and wall friction. Applied Mathematics and Mechanics, 38: 815-830, 2017.

[19] Md Abdus Sattar. Derivation of the similarity equation of the 2-d unsteady boundary layer equations and the corresponding similarity conditions. American Journalof Fluid Dynamics, 3(5): 135, 2013.